Article:

Keylock, C.J., Ganapathasubramani, B., Monty, J. et al. (2 more authors) (2016) The coupling between inner and outer scales in a zero pressure boundary layer evaluated using a Hölder exponent framework. Fluid Dynamics Research, 48 (2). 021405. ISSN 0169-5983

https://doi.org/10.1088/0169-5983/48/2/021405

The coupling between inner and outer scales in a zero pressure boundary layer evaluated using a Hölder exponent framework

Christopher J. Keylock[1a], Bharath Ganapathasubramani[2],
Jason Monty[3], Nick Hutchins[3] and Ivan Marusic[3]
[1]*Sheffield Fluid Mechanics Group and Department of Civil and Structural Engineering, University of Sheffield, Mappin Street, Sheffield, S1 3JD, UK*
[2] *Engineering and the Environment, University of Southampton, Southampton, SO17 1BJ, UK and*
[3] *Department of Mechanical Engineering, Parkville, University of Melbourne, 3010, Australia*

(Dated: March 8, 2016)

Abstract

This work considers the connectivity between large and small scales in boundary-layer turbulence by formalising the modulation effect of the small scales by the large in terms of the pointwise Hölder condition for the small scales. We re-investigate a previously published dataset from this perspective and are able to characterise the coupling effectively using the (cross-)correlative relations between the large scale velocity and the small scale Hölder exponents. The nature of this coupling varies as a function of dimensionless distance from the wall based on inner-scaling, y^+, as well as on the boundary-layer height, δ. In terms of the fundamental change in the sign of the coupling between large and small scales, the critical height appears to be $y^+ \sim 1000$. Below this height, small scale structures are associated with (and occur earlier than) maxima in the large scale velocity. Above this height, while the lag is similar in magnitude, the small scale structures are associated with minima in the large scale velocity. To consider these results further, we introduce a modified quadrant analysis and show that it is the coupling to the large scale low velocity state that is critical for the dynamics.

[a] Corresponding author: c.keylock@sheffield.ac.uk

I. INTRODUCTION

An improved understanding of high Reynolds number, boundary-layer turbulence is essential for both control purposes and developing enhanced numerical modelling methods for near-wall regions. Recent work in this field has focused on three inter-related areas: the formation of near-wall coherent flow structures [5, 30]; the nature of very large scale motions (VLSMs) in the outer part of the boundary-layer [1, 17, 51]; and, the coupling between these [11, 18]. See Jiménez [21] for a recent review of relevant work in these areas. The idea that the effect of large scale structures extends to the wall goes back at least as far as Townsend [52]. More recent work has shown that an important means by which coupling takes place is in the amplitude modulation of the small scales by the large [12, 18], and this has resulted in models for near-wall behavior based on knowledge of the VLSMs in the outer region [37].

In this study, rather than examining two-point statistics (near and far from the wall), we focus on the relation between large and small scales at a given height from the wall, y, and how this relation varies with y. The primary novelty in this work is an analysis of the amplitude modulation in terms of Hölder exponents. This means that we can move away from analyses predicated on discretised variables for the modulation such as the windowed variance of the small scale velocity to consider a continuous measure of the small scale modulation- its Hölder condition. Hence, with this change, it becomes straightforward to use standard techniques to examine the relation between the large-scale velocity and the small-scale modulation. We then study this as a function of distance from the wall, leading to a characterization of the phase relations between the large scale velocity and the Hölder exponents for the small scale intermittency. This permits an analysis of boundary-layer structure in terms of quadrants defined by the fluctuating velocity at large scales, and the Hölder exponents at small scales.

Hence, the plan for this paper is to review definitional information on Hölder exponents in section 2, describe the experimental facility and the data employed in this study, which have been published previously [12, 19], and to then give details of the signal pre-processing methods and the metrics used to characterize the relations between small and large scales in section 3. The results are then presented in section 4 and it is shown that the Hölder exponent approach is a natural way to elucidate the characteristics of boundary-layer velocity time series as a function of vertical coordinate, y.

II. POINTWISE HÖLDER EXPONENTS AND THEIR ESTIMATION

Landau's objection to Kolmogorov's original scaling 'law' for the moments of the velocity increments, or structure functions, in turbulence [9, 31] resulted in modified scalings that permitted intermittent behavior within the formulation [32, 49]. This intermittency was subsequently interpreted as a consequence of the presence of vortical structures in the flow [10]. A formal means of characterizing intermittency in turbulence was then introduced in terms of the multifractality of the flow field, or the sets of Hölder exponents present in the measured field [38, 39]. More correctly, we are interested in pointwise Hölder exponents, α_u of velocity time series data, rather than examining oscillating singularities [43], which requires the use of local Hölder exponents [2, 15, 33].

The general definition of α_u proceeds from consideration of the differentiability of a function relative to polynomial approximations about a location of interest, t_0. However, for turbulence in the inertial regime, where the mean, $\langle \alpha_u \rangle = \frac{1}{3}$ [31], then $0 < \alpha_u(t) < 1$ and one may consider, more simply, that

$$\alpha_u(t) = \sup\left\{\beta, \limsup_{\Delta_t \to 0} \frac{|u(t_0+\Delta_t) - u(t_0)|}{|\Delta_t|^\beta} = 0\right\} \tag{1}$$

where Δ_t is some interval about t_0. A rapid method for evaluating α_u is based on a log-log regression of the signal oscillations, $O_{t_0 \pm \Delta_t}$ against Δ_t [33]:

$$O_{t_0 \pm \Delta_t} = \max\left(u_{t \in (t_0 - \Delta_t, \ldots, t_0 + \Delta_t)}\right) - \min\left(u_{t \in (t_0 - \Delta_t, \ldots, t_0 + \Delta_t)}\right) \tag{2}$$

and in the evaluation of the α_u, Δ_t is distributed logarithmically (over limits from close to the Kolmogorov scale to inertial scales in this study to separate small and large scale behaviors). As explained by Peltier and Levy Véhel [45], our approach can be linked to the study of windowed variance (σ_u^2) approaches because

$$\frac{u_{t+\Delta_t} - u_t}{\Delta_t^{\alpha_u}} \underset{\Delta_t \to 0}{\to} N(0, \sigma_u^2) \tag{3}$$

where $N(\ldots)$ is the normal distribution. The left-hand side of eq. (3) then shows why eq. (2) is an appropriate means to estimate the Hölder exponent: the log-log regression probes the $\Delta_t \to 0$ limit that gives α_u. This approach has been shown to be at least as precise as alternative, wavelet-based methods [26], and has been used to infer the existence of "active periods" of shear stress exertion and sediment mobility from single-point time series in environmental/geophysical fluid mechanics studies [24, 25]. Because we are interested in deriving pointwise Hölder exponents, $\alpha_u(t)$ for 400 time series, each consisting of $N = 1.8 \times 10^6$ values, a rapid approach to Hölder exponent evaluation is of significant benefit, meaning that eq. (2) is adopted in this study.

A. Pointwise Hölder Exponents, Multifractality and Structure Functions

There has been a long history in turbulence of studying the moments of velocity increments, $u_{\Delta x} = u(x+\Delta_x)-u(x)$, [31, 55]. Given a power-law scaling between the nth moment $u^n_{\Delta x}$ and Δx with exponent ξ_n, a monofractal signal will exhibit a linear scaling between the moment order, n, and ξ_n [31], while a multifractal turbulence signal will exhibit a convex structure function relation [9]. Multifractality may also be considered directly from an analysis of $\alpha_u(x)$. For each possible $\alpha_u(t)$, we define the singularity spectrum, $D(\alpha_u)$ as the set of values for α_u for which the set S_{α_u} is not empty. The Frisch-Parisi conjecture states that

$$D(\alpha_u) = \min_n(\alpha_u n - \xi_n + 1) \tag{4}$$

Following Jaffard [20], in a window, $|\Delta_x|$ about a singularity of order α_u, one finds that

$$|u(x + \Delta_x) - u_x|^n \approx |\Delta_x|^{\alpha_u n} \tag{5}$$

Hence, for the second moment, $n = 2$, and assuming $\alpha_u = \langle\alpha_u\rangle$ everywhere, the Kolmogorov 2/3 law is recovered exactly when $\langle\alpha_u\rangle = 1/3$ as stated above.

With a dimension to these singularities of $D(\alpha_u)$ it follows that there are approximately $|\Delta_x|^{-D(\alpha_u)}$ boxes with a volume $|\Delta_x|^m$ where m is the dimension of the space over which the function is defined. Hence, the contribution of this singularity to the integral used to evaluate the structure function $\langle|u_{\Delta x}|^n\rangle$ is approximately $|\Delta_x|^{\alpha_u n+m-D(\alpha_u)}$. The largest contributor to the integral will be given by the smallest exponent. Thus,

$$\langle|u_{\Delta x}|^n\rangle \propto |\Delta_x|^{\xi_n} \tag{6}$$

$$\xi_n = \min_n(\alpha_u n - D(\alpha_u) + m) \tag{7}$$

That is, the structure function scaling exponent, ξ_n and the pointwise Hölder exponents, α_u, are related via the Legendre transform. More typically, we know ξ_n and are trying to estimate $D(\alpha_u)$. Thus, we need to take the inverse Legendre transform, which for a $m = 1$

dimensional signal yields eq. (4). While the velocity increments are defined over Δ_x, such quantities are not readily accessible using traditional instrumentation such as hot wires. Hence, spatial derivatives are usually obtained from time series using Taylor's hypothesis. While modified variants of this hypothesis have been formulated for flows where the action of large scale structures and, hence, local accelerations may be significant [22, 48], in this study we prefer to avoid any ambiguity that may result from the choice of transformation and work with time series (hence, u_t and $\alpha_u(t)$).

III. METHODS

A. Experimental Details

The data for this study came from an experiment at the high Reynolds number boundary layer wind tunnel at the University of Melbourne, Australia. The working section is 27 m long, with a 2×1 m cross-section. Additional details on this facility may be found in Nickels et al. [41] and Nickels et al. [42]. A summary of the experimental conditions is given in Table I and the basic unconditional statistics (e.g. mean and r.m.s. velocity profiles) are shown in Hutchins et al. [19]. The shear velocity is denoted by U_τ and use of the (+) superscript indicates a viscous, wall-unit scaling such that $t^+ = tU_\tau^2/\nu$ and $y^+ = yU_t/\nu$. The two Reynolds numbers quoted are the Kárman number, $\mathrm{Re}_\tau = \delta U_\tau/\nu$ and the momentum thickness number, $\mathrm{Re}_\theta = \theta U_\infty/\nu$. To give a sense of the behaviour of the Taylor Reynolds numbers, values at $y^+ \sim \{30, 200, 400\}$, i.e. top of the buffer layer, top of the inner layer and halfway into the outer layer, were $\mathrm{Re}_\lambda \sim 200, 280$ and 380, respectively.

Data were acquired at 60 kHz, twenty one meters into the working section. For the inflow condition used here ($U_\infty = 20.33$ ms^{-1}) the variation in the pressure coefficient along the working section was ± 0.007. Data were obtained from a hot-wire probe with an etched sensor length of 0.5 mm and wire diameter of 2.5 μm to give a length to diameter ratio of 200 [35]. The hot wire operated in constant temperature mode and was mounted 220 mm upstream of a traversable mount with an aerofoil profile to minimize flow disturbance [12]. The vertical traverse was precise to 0.1 μm and 40 logarithmically distributed vertical traverse positions were adopted in the range $0.24 < y < 450$ mm, with a boundary-layer thickness of 0.326 m ($y^+ = 14500$). The sampling period at each position was 30 s and ten

TABLE I. The experimental conditions for this study.

U_∞	U_τ	δ	Re_τ	Re_θ	t^+	min. y, (y^+)	max. y, (y/δ)
ms^{-1}	ms^{-1}	m	(-)	(-)	(-)	mm, (-)	mm, (-)
20.33	0.665	0.326	14200	36980	0.47	0.2 (10.67)	450 (1.38)

replicates were obtained at each sampling position.

B. Signal preprocessing

To study the interaction between small and large scales in these data Ganapathisubramani et al. [12] made use of a spectral filter so that the scale separation was precise in frequency. Previous studies using a box filter [6, 14] result in a separation that is precise in time/space rather than frequency. To avoid these two extreme cases, here we filter with a Daubechies least asymmetric wavelet filter with $L = 8$ non-vanishing moments [8], implemented within a maximal overlap discrete wavelet framework (MODWT) [23, 46]. We reconstruct the high frequency variability from wavelet scales, $j = 1, \ldots, 6$, and the large scales from $8 \leq j \leq J$, $j \in \mathbb{Z}$. As the equivalent filter width at scale j is given by $L_j = (2^j - 1) \times (L-1) + 1$, $j = 6$, 7, and 8 are equivalent to $t^+ = 208$, 418 and 839, respectively, where $t^+ = tU_\tau^2/\nu$, ν is the kinematic viscosity, and U_τ is obtained from a Clauser fit with $\kappa = 0.41$ and intercept $A = 5.0$ [7]. In terms of outer scaling, $tU_\infty/\delta = 0.46$, 0.93, and 1.86 for $j = 6, 7$, and 8, respectively, where U_∞ is the free stream velocity and δ is the boundary layer thickness. Based on the vertical structure of the energy spectra for u shown in Fig. 1 of Ganapathisubramani et al. [12], $tU_\infty/\delta = 1.86$ is close to an optimal separation of large and small scales for these data, while the $j \leq 6$ criterion for the small scales ensures a clear scale separation. Reconstruction from the wavelet coefficients by setting scales $j \geq 8$ to zero for the small scales, and $j \leq 6$ to zero for the large scales, and performing the inverse MODWT leads to the small and large scale velocity signals, $u_{\delta<}(t)$, and $u_{\delta>}(t)$, respectively. The pointwise Hölder exponents of the former are then denoted by $\alpha_{\delta<}(t)$.

An example short segment of $u_{\delta>}(t)$ (black line), $u_{\delta<}(t)$ (gray line in the upper panel) and $\alpha_{\delta<}(u)$ (gray line in the lower panel) is given in Fig. 1. Each is expressed in terms of a z-score, e.g. $z(u_{\delta>}) = (u_{\delta>} - \langle u_{\delta>} \rangle)/\sigma(u_{\delta>})$, where the braces indicate a temporal mean value and $\sigma(\ldots)$ is the standard deviation. It is clear that the larger scale behavior is

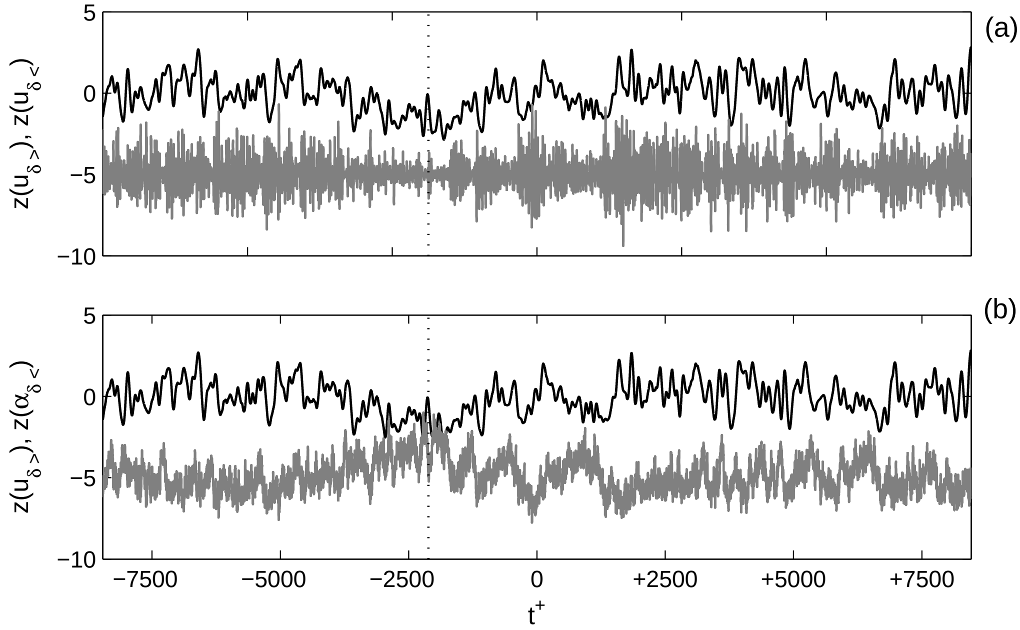

FIG. 1. Time series of $u_{\delta>}(t^+)$ (black), and $u_{\delta<}(t^+)$ (gray) in panel (a), and $u_{\delta>}(t^+)$ (black), and $\tilde{\alpha}_{\delta<}(t^+)$ (gray) in panel (b) for data from $y^+ = 10.64$. Values are expressed as normalized z-scores with data for the fine scales displaced by -5 for clarity. The origin for the timescale is arbitrary and the vertical dotted line at $t^+ \sim -2000$ highlights a feature identified in the text.

modulating the amplitude of $u_{\delta<}(t)$ in the top panel as highlighted by the vertical dotted line at $t^+ \sim -2000$ where the low values for $u_{\delta>}$ result in a reduced local variance for $u_{\delta<}$. This modulation is clearly captured by the dramatic increase in values for $\alpha_{\delta<}(t)$ in the lower panel at this point in time. The increase in $u_{\delta>}$ towards $t^+ = 0$ results in an increasing amplitude of the $u_{\delta<}$ signal and a concomitant decrease in $\alpha_{\delta<}$.

C. Analysis of filtered and unfiltered $\alpha_{\delta<}(t)$ values

Given $\alpha_{\delta<}(t)$, one can either consider its relation directly to $u_{\delta>}(t)$, or acknowledge that the impact of the difference in intrinsic timescales will introduce a decorrelation bias that will have a deleterious impact on the results. This then implies that $\alpha_{\delta<}(t)$ is low-pass filtered to the same cut-off frequency as $u_{\delta>}(t)$ before analysis. In the rest of this paper, we denote this filtered α series by $a_{\delta<}(t)$. Such a filtering removes the decorrelation bias, but also removes the noise associated with attempting to evaluate pointwise Hölder exponents for a discretely sampled dataset. Our approach is to primarily work with $a_{\delta<}(t)$, but to demonstrate at the start of the paper that the use of $\alpha_{\delta<}(t)$ gives qualitatively similar results, although with a reduced magnitude for the associated metric owing to both the decorrelation from timescale differences, and greater noise in the unfiltered data.

D. Metrics for large and small scale coupling

Given $\alpha_{\delta<}$ or $a_{\delta<}$ contains the information on the amplitude modulation, a simple metric for the coupling between large and small scales is the linear correlation between $u_{\delta>}$ and $\alpha_{\delta<}$, or $a_{\delta<}$, termed, for example, $R(u_{\delta>}, \alpha_{\delta<})$. The linear correlation is the covariance of the two variables normalized by the product of their standard deviations. To detect a time-lagged coupling, we apply the Hilbert transform to $u_{\delta>}$ and the Hölder series to evaluate the instantaneous phase of each signal and, thus, the phase difference. We define the analytical signal of a time varying, mean-subtracted, generic flow variable, $w^{'}(t)$, as $w^{'}(t) + i\hat{w}^{'}(t) = Ae^{i\phi_w}$, where $\hat{w}^{'}(t)$ is the Hilbert transform of $w^{'}$:

$$\hat{w}^{'} = \frac{1}{\pi}\text{p.v.}\int_{-\infty}^{+\infty} \frac{w^{'}(\breve{t})}{t-\breve{t}} d\breve{t}, \tag{8}$$

p.v. is the Cauchy principal value and $\breve{t}$ is the dummy integration variable. The phase is given by $\phi_w(t) \equiv \phi_{w^{'}}(t) = \tan^{-1}\frac{\hat{w}^{'}}{w^{'}}$, where we drop the prime for a fluctuating quantity for notational simplicity. It then follows that $R(\phi_{u>}, \phi_{\alpha<})$ is the linear correlation between the phases for $u^{'}_{\delta>}$ and $\alpha^{'}_{\delta<}$. The phase difference is then given by $\Delta\phi_{u,\alpha}(t) = \phi_{u>}(t) - \phi_{\alpha<}(t)$. Because the phase is defined on the unit circle, its mean value cannot be found using standard arithmetic averaging. Therefore, the mean phase coherence is found by averaging the angular distribution of phases on the unit circle in the complex plane [34]:

$$\gamma(\alpha) = \left| \frac{1}{N} \sum_{\Delta t=1}^{N} e^{i\Delta\phi_{u,\alpha}(t)} \right|. \tag{9}$$

where N is the number of samples in the time series, and Δt is the discrete time index for each sample. The distribution of γ is not uniform and to check that the value obtained is statistically meaningful we adopt a simple surrogate data approach. Such a process is implemented by phase-shuffling one of the time series before the phase differences are calculated. The mean value of γ for each of the surrogate series, γ_S, is denoted by $\langle\gamma_S\rangle$, and is used to normalize the value of γ from the data, where we obtain $\langle\gamma_S\rangle$ over ten surrogate series:

$$\gamma^*(\alpha) = \begin{cases} 0 & \text{if } \gamma < \langle\gamma_S\rangle \\ \frac{\gamma-\langle\gamma_S\rangle}{1-\langle\gamma_S\rangle} & \text{if } \gamma \geq \langle\gamma_S\rangle \end{cases} \tag{10}$$

An alternative way to explore properties of $\Delta\phi_{u,\alpha}(t)$ is to calculate its relative entropy, E_r. We divide the interval from -2π to $+2\pi$ into $b = \ldots, 200$ equal interval bins and obtain the empirical probabilities from $p_{\Delta\phi}(b) = n(b)/N$, where $n(b)$ is the number of values for $\Delta\phi_{u,\alpha}$ in a given interval. The relative entropy is then given by

$$E_r(\Delta\phi_{u,\alpha}) = \frac{\sum_{i=1}^{b} p_{\Delta\phi} \log p_{\Delta\phi}}{\log \frac{1}{b}} \tag{11}$$

Hence, $E_r(\Delta\phi_{u,\alpha}) > 1$ indicates greater order than for an equivalent uniform distribution and, thus, a tendency for preferential values for the phase difference between the large scale velocity and small scale Hölder exponents to arise. Thus, overall, we have four metrics for both $\alpha_{\delta<}$ and $a_{\delta<}$, e.g.: $R(u_{\delta>}, \alpha_{\delta<})$, $R(\phi_{u>}, \phi_{\alpha<})$, $\gamma^*(\alpha)$, and, $E_r(\Delta\phi_{u,\alpha})$.

E. Velocity-Intermittency Quadrant Analysis

We also make use of a velocity-intermittency quadrant analysis to gain a greater insight into this coupled behavior, although it is applied in a different fashion to the original formulation in Keylock et al. [27]. In that work, the intention was to examine any dependence in the intermittency time series on the velocity, where it is classically assumed, e.g. [32], that no such dependence exists (although, see Hosokawa [16] and Stresing and Peinke [50]). A simple method was developed to examine this dependence based on renormalized quantities and the well-known quadrant method in boundary-layer fluid mechanics [3, 36]. Hence, the joint distribution function for $z(u)$ and $z(\alpha_u)$ was examined as a function of a threshold 'hole size', with a significant event for a given H one where $|z(u)z(\alpha_u)| \geq H$. By increasing H from 0 to a maximum given by associated sampling theory for the Gaussian distribution for a given N and counting the proportion of events in each quadrant, $p_Q(H)$, different type of flow (jets, wakes, boundary layers near and far from the wall) could be discriminated readily. Further work highlighted that the flow over bed roughness elements (mobile and fixed) generated a velocity-intermittency structure different to that for any of the more idealized flow types [28, 29].

In this study, we modify this technique to determine the relation between $u_{\delta>}(t)$ and $a_{\delta<}(t)$, i.e. the coupled behavior of large scale velocity and filtered small scale intermittency.

TABLE II. The definition of velocity-intermittency quadrants in terms of the signs of $u'_{\delta>}$ and $a'_{\delta<}$.

Quadrant number (Q)	sgn($u'_{\delta>}$)	sgn($\alpha'_{\delta<}$)
1	+	+
2	-	+
3	-	-
4	+	-

TABLE III. The proportion of the data exceeding the thresholds shown in Fig. 2 for each quadrant. Results are re-normalized such that the total proportion always sums to 1.0.

Quadrant number (Q)	$H = 0$	$H = 1$	$H = 2$	$H = 3$
1	0.157	0.052	0.012	0.002
2	0.314	0.456	0.538	0.575
3	0.207	0.073	0.017	0.004
4	0.322	0.419	0.433	0.420

The four quadrants are defined according to Table II, with an example diagram shown in Fig. 2. This makes use of the data in Fig. 1 and, consequently, is based on $\alpha_{\delta<}(t)$ rather than $a_{\delta<}(t)$. It is clear that in this case, as H increases, $Q = 2$ and $Q = 4$ are increasingly dominant, with this being particularly the case for the former quadrant. This is made explicit in Table III, which gives the proportion of data exceeding the H thresholds shown in Fig. 2. Hence, for these data near the wall ($y^+ = 10.67$) there is a negative correlation between $u_{\delta>}(t)$ and $\alpha_{\delta<}(t)$, meaning that for $H \gtrsim 2$ there are essentially two states that arise 97% of the time: a slower than average large scale velocity coupled to a smoother than average small scale velocity signal ($Q = 2$), and a faster than average large scale velocity coupled to a rougher than average small scale velocity signal ($Q = 4$).

It was found previously that because of the approximate linear variation of p_Q with H for a given quadrant, dp_Q/dH could be used as a summary measure for the behavior of the flow in each quadrant [29]. This approximation is used here to show how velocity-intermittency response varies as a function of y^+.

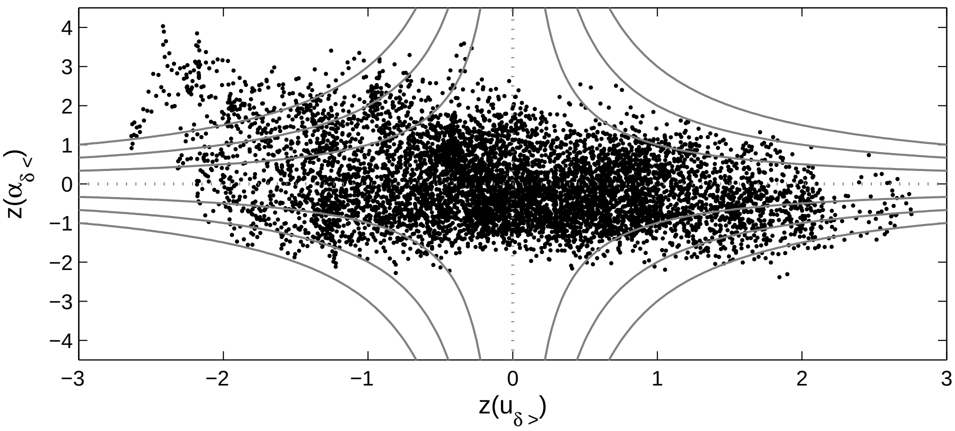

FIG. 2. An example velocity-intermittency quadrant diagram for $u_{\delta>}$ and $\alpha_{\delta<}$ using the data from Fig. 1. Contours for $H \in \{1, 2, 3\}$ are shown as gray lines.

IV. RESULTS

A. Summary Measures of Large and Small Scale Coupling

Figure 3 shows the average over the ten replicates (indicated by angle braces) of the coupling metrics defined in section 3 as a function of y^+, using the unfiltered Hölder exponents. The two synchronization methods are shown in panels (b) and (d), and both show a strongly expressed peak in the coupling at $y^+ \sim 10^4$. However, while $\langle E_r \rangle_\alpha$ is approximately constant for $10 < y^+ < 3000$, $\langle \gamma^* \rangle_\alpha$ halves in value over the same range. The results for the two correlation metrics are entirely consistent, with a move from negative to positive correlations as y^+ increases until a maximum is reached just before $y/\delta = 1$. In both cases, the zero-crossing for the correlation coefficient takes place close to $y^+ = 300$, values increase to $y^+ \sim 10^4$ and then, outside the boundary layer, the correlation drops to zero. Thus, near the wall, high values for $u_{\delta>}$ result in high local variation for $u_{\delta<}$ (low $\alpha_{\delta<}$ and negative correlation), with the opposite the case for $y^+ \gtrsim 300$.

Replacing $\alpha_{\delta<}(t)$ by $a_{\delta<}(t)$ gives the results shown in Fig. 4, which are generally consistent with those in Fig. 3. The magnitude of the negative correlations at $y^+ \sim 10$ is three times greater than for $\alpha_{\delta<}(t)$, while the peak positive correlations at $y^+ = 10000$ are approximately twice as large, indicating the degree of decorrelation that results from the analysis of time series with different intrinsic time scales. The zero-crossing of these correlation coefficients is

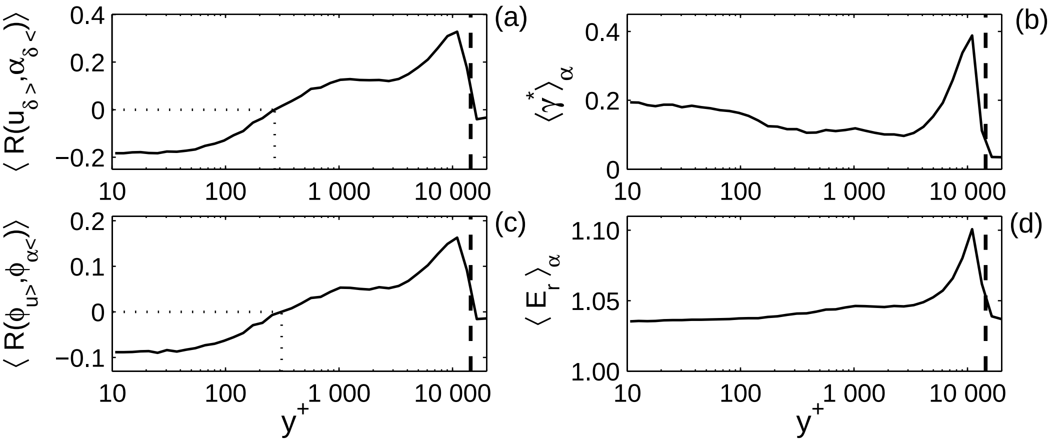

FIG. 3. Mean over ten replicates of four different metrics of the coupling between $u_{\delta>}(t)$ and $\alpha_{\delta<}(t)$ as a function of y^+. The zero-crossing of the two correlation metrics is shown with dotted lines, while the vertical dashed line is at $y/\delta = 1$.

displaced to $y^+ \sim 500$ and a similar, rapid decay to zero correlation for $y/\delta > 1$ is observed. Similarly to Fig. 3b, $\langle \gamma^* \rangle_a$ halves in value over $10 < y^+ < 3000$, attaining a minimum at the same position as before, before rapidly increasing to a peak close to $y/\delta = 1$. The major difference in the results is the inversion of the peak in $\langle E_r \rangle_a$ at a similar y^+. It should be noted that the value for $\langle E_r \rangle_a$ in this trough is still greater than that for the peak in Fig. 3d. However, this clear contrast to the result in Fig. 4b indicates a different development in the shape of the PDF for $\Delta\phi_{u,a}$ at $y^+ \sim 10000$ relative to the phase synchronization between $u_{\delta>}(t)$ and $\alpha_{\delta<}(t)$, which is explored further in section 4.3. Thus, for $10 < y^+ < 3000$, $\langle E_r \rangle_a \equiv \langle E_r(\Delta\phi_{u,a}) \rangle$ is approximately constant but the phase synchronization decreases. This can be contrasted to Fig. 3b,d where the decrease in $\langle \gamma^* \rangle_\alpha$ with y^+ in this range is accompanied by an increase in $\langle E_r \rangle_\alpha$, with both attaining a local maximum at $y^+ \sim 10000$.

B. Extending the Correlative Measures to Cross-Correlations

The assumption of zero lag in the correlations in Fig. 3a and 4a is a strong one and there is some visual evidence for a lagged response in Fig. 1. To investigate this further, the $R(u_{\delta>}, \alpha_{\delta<})$ values were generalized to a cross-correlation function, $R(u_{\delta>}, \alpha_{\delta<}, \Delta_t^+)$ over all $2N - 1$ lags, Δ_t, expressed in wall units as $\Delta_t^+ = \Delta_t U_\tau^2/\nu$. Figure 5 shows the mean over the ten replicates of the signed maximum absolute cross correlation and the lag to this

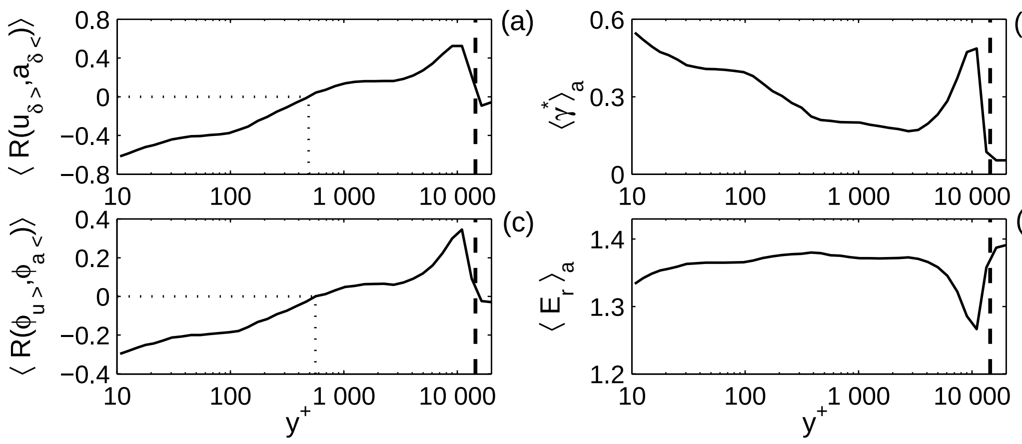

FIG. 4. Mean over ten replicates of four different metrics of the coupling between $u_{\delta>}(t)$ and $a_{\delta<}(t)$ as a function of y^+. The zero-crossing of the two correlation metrics is shown with dotted lines, while the vertical dashed line is at $y/\delta = 1$.

correlation. By way of example, for the unfiltered Hölder series, this is given by

$$\begin{aligned} \mathrm{sgn}(R_{max}) \times |R|_{max} &= \mathrm{sgn}(\max|R(u_{\delta>}, \alpha_{\delta<}, \Delta t^+)|) \\ &\quad \times \max|R(u_{\delta>}, \alpha_{\delta<}, \Delta_t^+)| \end{aligned} \tag{12}$$

as well as the associated lag:

$$\Delta t^+_{\max} = \arg\max_t R(u_{\delta>}, \alpha_{\delta<}, \Delta_t^+) \tag{13}$$

where a positive lag indicates that a change in $\alpha_{\delta<}$ leads $u_{\delta>}$. Confidence limits at the 95% level are placed on these results using the bootstrap procedure outlined in the appendix. Insignificant values for $\Delta t^+_{\max}$ based on the results in panel (a) are highlighted by solid symbols in Fig. 5(b).

As in Fig. 3 and 4, the correlations reported in Fig. 5a change from negative to positive with increasing y^+, although the point of transition is now higher into the flow than was the case in Fig. 3. It also occurs at a similar value of y^+ for both the filtered and unfiltered Hölder series. That this transition is very similar to that seen in Fig. 4 suggests that filtering the Hölder series yields more physically interpretable results as there is a greatly reduced dependence on Δt^+. This is borne out directly in Fig. 5b, which shows $\Delta t^+_{max} \sim 0$ for all y^+ where the results are significant except for the data adjoining the region of no significance, where the magnitude of the peak correlations is much reduced. The results

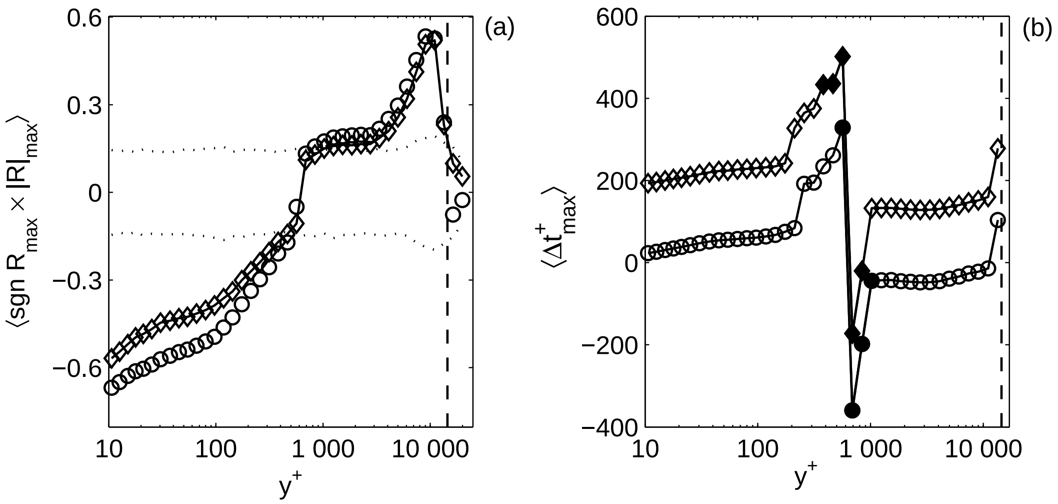

FIG. 5. Mean over ten replicates of $\mathrm{sgn}(R_{max}) \times |R|_{max}$ as a function of y^+ (a), and the time lag to this maximum, Δt^+_{max} (b). Results shown with a diamond are for $R(u_{\delta>}, \alpha_{\delta<}, \Delta t^+)$, while those with a circle are for $R(u_{\delta>}, a_{\delta<}, \Delta t^+)$. The vertical, dashed line shows $y/\delta = 1$ and the approximately horizontal lines in (a) are 95% confidence intervals based on a bootstrapping of the $R(u_{\delta>}, \alpha_{\delta<})$ results. Results that are insignificant in (b) based on those in (a) are highlighted by solid symbols.

in Fig. 5a highlight a break in slope of the variation of the cross-correlation at $y^+ \sim 100$, followed by a rapid decrease in correlation magnitude with height until $y^+ \sim 1000$, which was also evident in Fig. 4a,b,c. A major difference between the results for $R(u_{\delta>}, a_{\delta<}, \Delta t^+)$ and $R(u_{\delta>}, \alpha_{\delta<}, \Delta t^+)$ in Fig. 5 is that for the former, significant positive correlations are associated with negative lags and vice versa (although the magnitudes of the lags are small), while lags remain positive for $R(u_{\delta>}, \alpha_{\delta<}, \Delta t^+)$.

What is of further note is that while the positive correlations in Fig. 3a, 4a, and 5a attain a magnitude at high y^+ that is not dissimilar to those near the wall, the phase synchronizations in Fig. 3c and 4c exhibits a decrease with height (rather than a global minimum close to the height of zero correlation). Hence, while linear measures of association imply that the boundary-layer is as structured close to $y/\delta = 1$ as it is at the wall, γ_a^* indicates that near-wall structure is more strongly expressed. We examine this qualitative difference further by explicitly referring to the phase differences.

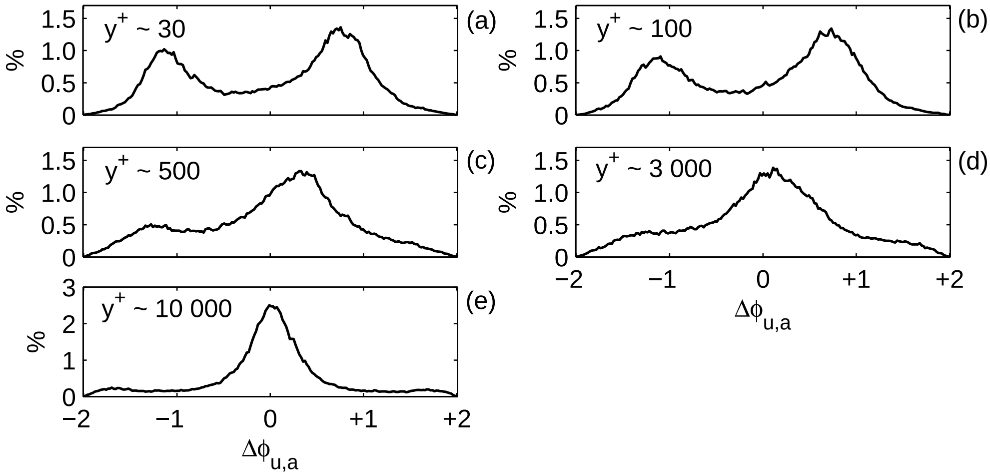

FIG. 6. Histograms of $\Delta\phi_{u,a}$ at choices for y^+ that have qualitatively different values for $\langle\gamma^*\rangle_a$ based on the results in Fig. 4. The dataset chosen is that closest to the median value for γ^* between $u_{\delta>}$ and $a_{\delta<}$.

C. Distribution functions of the phase difference

The histograms for $\Delta\phi_{u,a}$ are shown in Fig. 6 for five choices of y^+ that exhibit differences in their values for $\langle\gamma^*\rangle_a$ according to the results in Fig. 4. The results at $y^+ \sim 3000$ correspond to the minimum for $\langle\gamma^*\rangle_a$ and Fig. 6d shows that the distribution for $\Delta\phi_{u,a}$ is unimodal, centered close to zero phase difference and that the central peak does not contain a particularly high proportion of the distribution's mass. Hence, this is the result closest to that obtained from random surrogate data, explaining the low value for $\langle\gamma^*\rangle_a$. In contrast, at $y^+ \sim 10000$ the greater kurtosis of the central mode is less attainable by random processes and both $\langle\gamma^*\rangle_a$ and $R(u_{\delta>}, a_{\delta<}, \Delta t^+)$ are greater. Nearer the wall, the bimodal nature of the histogram for $\Delta\phi_{u,a}$ explains the decline in $\langle\gamma^*\rangle_a$ with y^+ despite similar magnitude values for $\mathrm{sgn}R_{max} \times |R|_{max}$ existing at $y^+ \sim 10000$ and $y^+ \sim 100$. For $y^+ > 100$ the right mode moves towards $\Delta\phi_{u,a} = 0$ and the left mode diminishes. Higher values for $\langle\gamma^*\rangle_a$ for $y^+ < 100$ are a consequence of a more defined mode in the left tail that could not be mimicked by random surrogates. Hence, the change from negative to positive correlations does not arise independently of the shape of the PDF for $\Delta\phi_{u,a}$ meaning that the physical explanation of the amplitude modulation of small scales by the large must also account for a transition from a bimodal to an unimodal response.

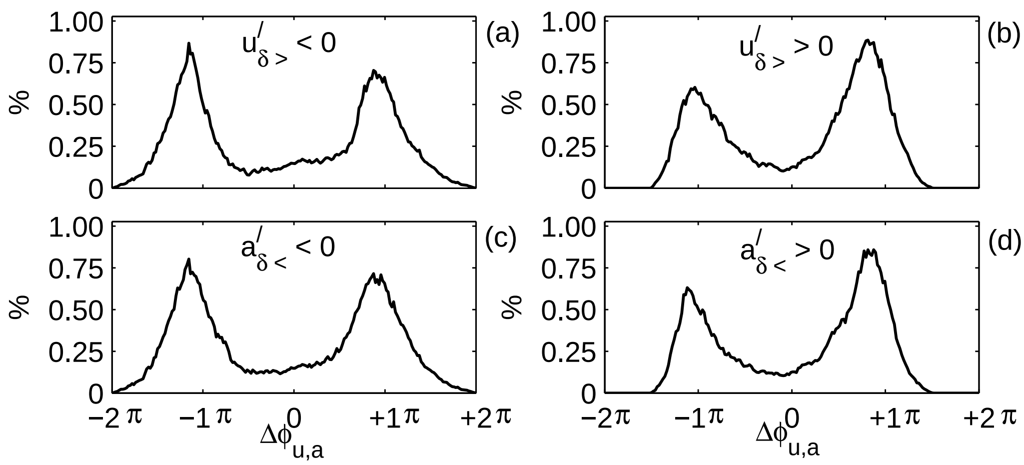

FIG. 7. Histograms of $\Delta\phi_{u,a}$ at $y^+ = 12.6$ conditioned on the sign of $u^{'}_{\delta>}$, (a) and (b), and the sign of $a^{'}_{\delta<}$, (c) and (d). The y-axis is expressed in terms of the full PDF for $\Delta\phi_{u,a}$.

The asymmetry in the near-wall peaks can be analysed further by conditioning $p(\Delta\phi_{u,a})$ on the sign of $a^{'}_{\delta<}$ or $u^{'}_{\delta>}$. For example, at $y^+ = 12.6$, 55% of the distribution's mass is in the upper part ($\Delta\phi_{u,a} > 0$), but there is a clear difference between $p(\Delta\phi_{u,a}|\mathrm{sgn}(a^{'}_{\delta<}) > 0)$ and $p(\Delta\phi_{u,a}|\mathrm{sgn}(a^{'}_{\delta<}) \leq 0)$, with 59.5% of the mass of the former in the positive phase difference region (Fig. 7d), compared to 51.2% for the latter (Fig. 7c). Interestingly, given the negative correlations near the wall seen in Fig. 4 and 5, it is $p(\Delta\phi_{u,a}|\mathrm{sgn}(u^{'}_{\delta>}) > 0)$ that also preferentially contains the positive phase differences (58.9% in Fig. 7b compared to 51.1% for $p(\Delta\phi_{u,a}|\mathrm{sgn}(u^{'}_{\delta>}) \leq 0)$ in Fig. 7a). Hence, there is a joint control on the phase differences from the two variables that does not reflect their negative correlation at this height. This demonstrates the relevance of velocity-intermittency quadrants for analysing this phenomenon and the suitably conditioned variables over the signs of both quantities, $p[\Delta\phi_{u,a}|\mathrm{sgn}(u^{'}_{\delta>}), \mathrm{sgn}(a^{'}_{\delta<})]$, are shown in Fig. 8. The normalization of the ordinate is according to the proportion of the unconditioned $p(\Delta\phi_{u,a})$ so that it is clear that the quadrants occupied the most are Quadrant 2 ($u^{'}_{\delta>} < 0, a^{'}_{\delta<} > 0$) and 4 ($u^{'}_{\delta>} > 0, a^{'}_{\delta<} < 0$), which is consistent with Fig. 2. This figure clarifies the potential confusion that results from comparing the correlation and the conditioning on single variables: quadrants 2 and 4 have a similar bimodal response and although they are frequented less often, it is quadrants 1 and 3 that explain the differences seen in Fig. 7. During periods of relatively fast, smooth flow at large scales (quadrant 1, Fig. 8b) a positive phase difference is twice as likely as a negative,

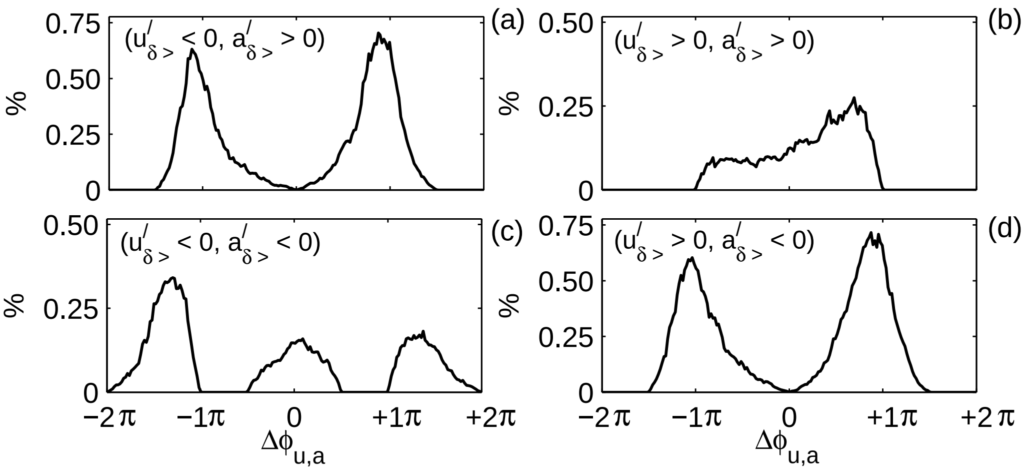

FIG. 8. Histograms of $\Delta\phi_{u,a}$ at $y^+ = 12.6$ conditioned simultaneously on the sign of $u^{'}_{\delta>}$ and the sign of $a^{'}_{\delta<}$. The y-axis is expressed in terms of the full PDF for $\Delta\phi_{u,a}$.

with all differences existing over a relatively narrow range of phases ($-\pi < p(\Delta\phi_{u,a}) < \pi$). Quadrant 3 exhibits an opposite response with both larger magnitude phase differences and a peak negative phase difference twice as great as the peak positive response. It was proposed by Marusic et al. [37] that the following model formulation could be used to predict near-wall flow based on the large scale fluctuations

$$u^+_P(y) = u^+_{BL}(y)(1 + k_1 u^+_{\delta>}(y)) + k_2 u^+_{\delta>}(y), \tag{14}$$

where all quantities are written in terms of wall units (+ superscript), the left hand term is the predicted velocity, u_{BL} is the "universal" signal at that height derived from the law-of-the-wall or similar, and the k are coefficients representing the modulation effect, k_1, and the superposition of the large scale influences, k_2. The results presented here suggest that a more advanced variant of this model would consider the joint velocity-intermittency behavior of the larger scales and constrain the modulation coefficient vector (for the various $\mathrm{sgn}(u_{\delta>}), \mathrm{sgn}(a_{\delta>})$ combinations) with respect to each case.

D. Velocity-intermittency quadrants

Given the relevance of the velocity-intermittency quadrants for examining the phase difference responses, we look more carefully at the quadrant occupany in this section by examining the gradient of the proportional occupany, p_Q, versus hole size, H, introduced by

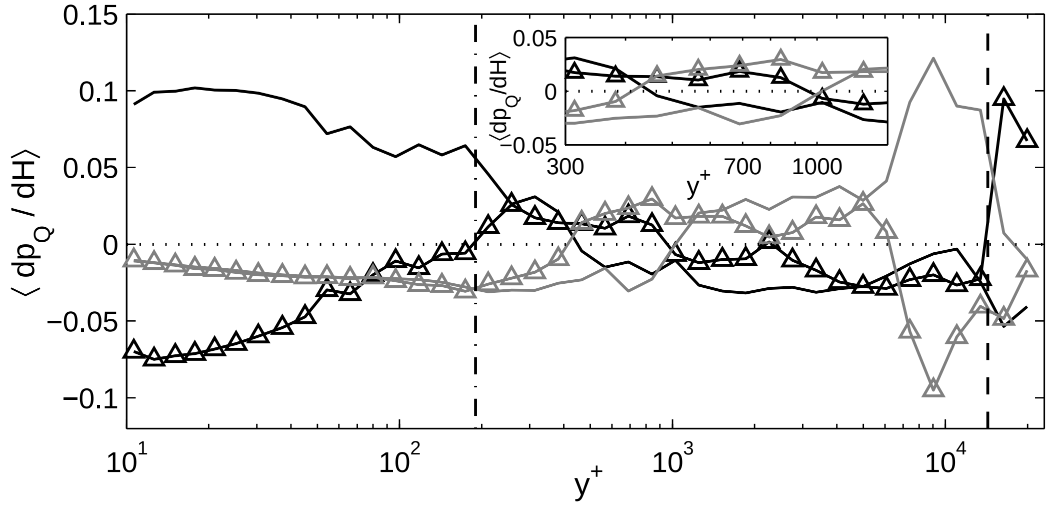

FIG. 9. The mean over ten replicates of the scaling between quadrant proportional occupany, p_Q, and hole size, H, for the four quadrants defined according to Keylock et al. [27]. The black line shows the behavior for quadrant 2, while the black line with triangles is quadrant 4. The gray line is quadrant 3 and the gray line with triangles is quadrant 1. The inset shows more clearly where the slopes of $\langle dp_Q/dH\rangle$ change sign. The horizontal dotted line is at $\langle dp_Q/dH\rangle = 0$, while the vertical dashed and dash-dotted lines are at $y/\delta = 1$ and $y^+ = 190$, respectively.

Keylock et al. [29]. The means over ten replicates for dp_Q/dH as a function of y^+ are shown in Fig. 9. Quadrants Q1 and Q3 exhibit almost identical behavior, with a linear increase (on a semi-log axis) in the strength of the negative slope for y^+ less than 190 (indicated by a vertical, dash-dotted line), i.e. in the inner wall region. This is also the value at which the sign for Q4 changes to positive. This quadrant has a stronger negative slope than Q1 and Q3 until $y^+ \sim 80$. For $y^+ > 190$ the Q2 contribution decays towards a zero-crossing at $y^+ \sim 450$ and then is approximately constant at $\langle dp_Q/dH\rangle \sim -0.04$, until $y^+ \sim 6000$. In general, for $250 < y^+ < 5000$ there are no strong variations in the quadrant occupancy with H, indicating a relatively stable velocity-intermittency relation at these heights.

Figure 10 shows the results at four elevations in greater detail to the dp_Q/dH summary measure in Fig. 9. The general patterns are in agreement with the above interpretation, with the situation at $y^+ = 174$ similar to that at $y^+ = 21$, but with less extreme slopes. In the former, at large H, the limiting state is $\sim 70\%$ occupancy in Q2 and $\sim 30\%$ in Q4, while the latter is close to 100% in Q2. In the mid-range of elevations, it is Q1 and Q3 that dominate in this limit with about 35% occupancy, and Q2 and Q4 contributing 15% each.

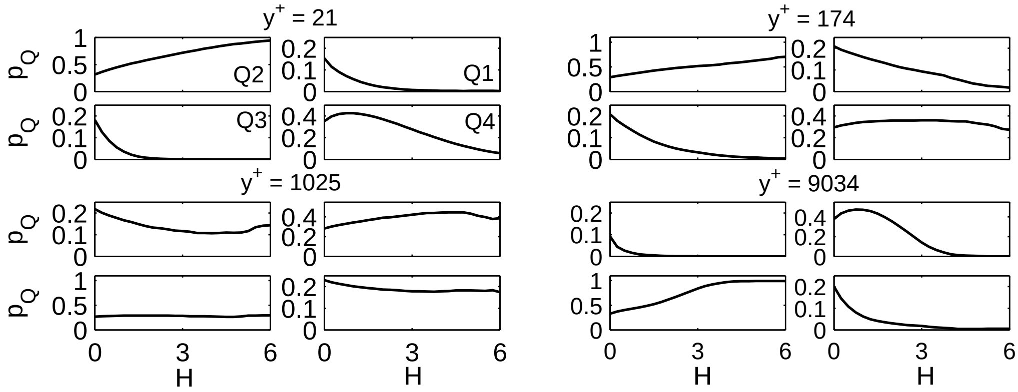

FIG. 10. Mean over ten replicates of the variation of p_Q with H in each of the four quadrants at four choices for y^+ selected on the basis of the results in Fig. 9.

However, at $y^+ = 9034$ s one approaches 100% occupancy in Q3 at large H. Hence, the manner in which the extreme flow states modulate the small scales changes with elevation:

- Near the wall, the key control is $u'_{\delta>} < 0$, which exerts a strong control on the $a'_{\delta<} > 0$, i.e. smooth regions of the flow where strain rates or vorticity are low;
- At $y^+ = 174$ this control is present, as well as the consistent, but opposite, control of $u'_{\delta>} > 0$ on $a'_{\delta<} < 0$;
- Further from the wall, where Reynolds stresses are lower and structures developed autogenically at the wall rarely penetrate, the control is inverted from that at $y^+ = 174$ with $u'_{\delta>} > 0$ affecting $a'_{\delta<} > 0$ and the lower velocity regions, $u'_{\delta>} < 0$, producing the regions of large fluctuations, $a'_{\delta<} < 0$; and,
- Nearer the boundary-layer height, the velocity control is again dominated by $u'_{\delta>} < 0$, but it controls $a'_{\delta<} < 0$ this time.

This result may be summarized as a negative velocity-intermittency correlation existing for $y^+ < 190$, and a positive one at higher elevations, with the refinement that very close to, or very far from the wall, it is one quadrant that dominates this relation.

V. DISCUSSION

That the Q2 dominance near the wall decays markedly from $y^+ > 190$ is coincident with the observation that attached hairpin vortices rarely penetrate beyond this height [13].

This implies that positive Q2 is related to these near-wall vortical processes, i.e. regions of reduced variance below the inertial scale are coupled to slower than average large-scale velocities, and this result dominates in the limit of large H. Single quadrant dominance in the results both near the wall (Q2) and near the top of the boundary-layer (Q3) implies that a correlation-based analysis is not sufficient: there is a sign change in the correlation between $u^{'}_{\delta >}$ and $a^{'}_{\delta <} > 0$ with height, but it is the $u^{'}_{\delta >} < 0$ states that drive this relation. It is clear from the phase analysis that the nature of the coupling near and far from the wall is very different, with a marked bimodality to the phase relations near the wall and a unimodal, zero phase lag response as one approaches $z/\delta = 1$. Figure 8 shows how the bimodality is linked to the quadrants with the positive lags associated with Q1, and the negative with Q3. Hence, although Q2 dominates near-wall response, other quadrants play an important part in shaping the detail of the coupling between large-scale velocity and small scale intermittency.

Assuming that, following Frisch et al. [10] regions with $\alpha_{\delta <} < 0$ indicate the passage of flow structure with a high vorticity, then near the bed, regions of limited vorticity at the small scales are coupled to a subsequent large scale velocity minimum that induces a large-scale strain. Hence, regions with weak vorticity are not passive in turbulence [53] and there is a suggestion here that the change from Q2 to Q3 dominance reflects a shift from small-scale energy dissipation driven by strain production near the wall to enstrophy production higher into the flow. This postulated behavior may be interpreted with respect to the geometric properties of the velocity gradient tensor, [44, 47, 54]:

$$A_{ij} = \begin{pmatrix} \partial u_1/\partial x_1 & \partial u_1/\partial x_2 & \partial u_1/\partial x_3 \\ \partial u_2/\partial x_1 & \partial u_2/\partial x_2 & \partial u_2/\partial x_3 \\ \partial u_3/\partial x_1 & \partial u_3/\partial x_2 & \partial u_3/\partial x_3 \end{pmatrix} \tag{15}$$

The characteristic equation for the velocity gradient tensor is $A_{ij} = e_i^3 + \mathrm{P}e_i^2 + \mathrm{Q}e_i + \mathrm{R} = 0$, where e_i are the eigenvalues of A. While incompressibility means that $\mathrm{P} = 0$, Q and R and their associated evolution equations are often studied:

$$\mathrm{Q} = \sum \delta_{ij} e_i e_j \equiv \frac{1}{4}(\omega^2 - 2\mathrm{S}^2) \tag{16}$$

$$\mathrm{R} = \prod e_i \equiv -\frac{1}{3} S_{ij} S_{jk} S_{ik} - \frac{1}{4}\omega_i \omega_j S_{ij} \tag{17}$$

where $\omega^2 = \omega_i \omega_i$ and the strain, S_{ij}, rotation, Ω_{ij} and vorticity, ω_{ij} are given by

$$S_{ij} = A_{ij} + A_{ij}^{\mathrm{T}} \tag{18}$$

$$\Omega_{ij} = A_{ij} - A_{ij}^{\mathrm{T}} \tag{19}$$

$$\omega_i = \epsilon_{ijk}\Omega_{jk} \tag{20}$$

where ϵ_{ijk} is the Levi-Civita symbol. It was shown by Naso et al. [40] using a DNS of a shear flow, the Vieillefosse tail [54] (i.e. the $R > 0$, $Q < 0$ flow state with high strain production and low vorticity) grew proportionally more than other regions of the $Q-R$ plane as dimensionless shear rate increased, i.e. the extreme cases of very high strain production and low vorticity became more likely. Given the high shear rates near the wall in a boundary layer, this is entirely consistent with our postulated predominance of a $R > 0$, $Q < 0$ flow state for $y^+ < 190$ that is coupled to velocity minima at large scales. As this region of the $Q-R$ plane is associated with small scale energy dissipation [4], we may link the Reynolds stress profile in a boundary layer with our Q2 dominance and the $R > 0$, $Q < 0$ flow state. Hence, the velocity-intermittency quadrant method, although based on pointwise velocity time series, permits interpretation of the results that are consistent with numerical results where A_{ij} has been resolved.

VI. CONCLUSION

Using a time series of pointwise Hölder exponents to characterize small scale turbulence provides an alternative means of studying the coupling between large and small scales in a zero-pressure turbulent boundary layer. Because this is a continuous measure with close theoretical links to structure function analysis and studies of turbulence multifractality, it has a logical basis for application in turbulence research. We have then applied correlative and phase-based metrics to characterise the relation between the large and small scale flow behavior. By modifying a recently developed velocity-intermittency quadrant analysis [27] such that the velocity axis is the low-pass filtered velocity and the intermittency is that detected at small scales, it has been shown that the crucial changes to the large and small scale coupling are driven by the times when the velocity at large scales is less than average. The reason that the correlation between large and small scales changes sign at $y^+ \sim 300$ is because of a change from an association between low velocities at large scales and less intermittent conditions at small scales, to one where the large scale, low velocities are linked to more intermittent conditions. Hence, it is the low velocity states both near and far from the wall that drive the relation between large and small scales, and the change in sign of the correlation as a consequence. The nature of the phase relations underpinning the correlation is also complicated, with bimodality in the phase differences near the wall and unimodality closer to the top of the boundary-layer. These results suggest modifications to the equation proposed by Marusic et al. [37] for characterizing near wall flow by modifying the boundary-layer profile to account for the modulation of the small scales by the large. Conditioning of such a model based on the velocity-intermittency quadrants has the potential to lead to more accurate results and this dimension of the present study will be explored further in future work.

Assuming that low values for the pointwise Hölder exponents relate to the presence of vortical flow structures [10, 24], we have detected a shift from large scale strain being coupled to low enstrophy production at small scales near the wall, to large scale strain relating to the presence of vortical flow structures (and high enstrophy production) at small scales further from the wall. Thus, although this work has been based purely on the analysis of velocity time series at a point, the changing nature of the coupling between scales as a function of height appears to be consistent with numerical analyses of enstrophy and strain production in a boundary-layer. That the joint analysis of large scale velocity and small scale Hölder exponents can provide similar insights provides an encouraging basis for further work using these tools.

Appendix A: Bootstrapped confidence intervals for cross-correlation analysis

An approach to bootstrapping confidence intervals on the maximum absolute cross-correlation between $u_{\delta>}$ and $\alpha_{\delta<}$ is useful because conventional hypothesis testing for cross-correlation assumes, as a null hypothesis, no autocorrelation in the underlying time series, giving a confidence interval proportional to the square root of the sample size, N and, thus, rapidly tending to zero. The approach followed here is to form the bounds from the cross-correlation of phase-randomized surrogate data that preserve the autocorrelative structure of each series, according to:

1. Take the Fourier transform of $u_{\delta>}(t)-\langle u_{\delta>}\rangle$ and $\alpha_{\delta<}(t)-\langle \alpha_{\delta<}\rangle$ and store the respective amplitudes, $A_u(\omega)$ and $A_\alpha(\omega)$;

2. Choose a significance level, s, such that the exceedance probability for the maxima

will be $\rho = 1 - s/2$;

3. For each of S surrogate series:

   (a) Randomly shuffle $u_{\delta>}$ and $\alpha_{\delta<}$, take the Fourier transform of each series and store the random phases, $\tilde{\phi}_u(\omega)$, and $\tilde{\phi}_\alpha(\omega)$, where the tilde indicates these are random quantities;

   (b) Take the inverse Fourier transform of $A_u \exp i\tilde{\phi}_u$ and $A_\alpha \exp i\tilde{\phi}_\alpha$ to yield phase-randomized data, $\tilde{u}_{\delta>}(t)$, and $\tilde{\alpha}_{\delta<}(t)$;

   (c) Find the maximum and minimum of the cross-correlation, $R(\tilde{u}_{\delta>}, \tilde{\alpha}_{\delta<})$, as a function of lag, Δt and add them to the vectors $\mathbf{X}$ and $\mathbf{N}$, containing the maxima and minima, respectively.

4. Fit a Generalized Extreme Value distribution to the S-element vectors $\mathbf{X}$ and $-\mathbf{N}$ and for the given fits, evaluate the distribution functions for $P(\mathbf{X})$ and $P(-\mathbf{N})$ at ρ. The bounds are then given by $R(u_{\delta>}, \alpha_{\delta<})^{\rho} = P(\mathbf{X}|\rho)$ and $R(u_{\delta>}, \alpha_{\delta<})^{1-\rho} = -P(-\mathbf{N}|\rho)$.

The use of a distribution function removes the explicit dependence on S, although clearly the estimation improves as $S \to \infty$. The results of a simulation study for a dataset at $y^+ = 690$ for $S \in \{25, 50, 75, 100\}$ are shown in Fig. 11, where twenty estimates for $R(u_{\delta>}, \alpha_{\delta<})^{\rho}$ and $R(u_{\delta>}, \alpha_{\delta<})^{1-\rho}$ are produced for each choice of S, with $\rho = 0.975$. Given that in this study, ten replicates were obtained at each value for y, a mean confidence limit can be obtained and the relatively constant standard error here indicates that $S = 25$ for each data series is sufficient.

---

[1] Adrian R J, Meinhart C D and Tomkins C D 2000 *J. Fluid Mech.* **422**, 1–54.

[2] Barrière O, Echelardy A and Lévy Véhel J 2012 *Electron. J. Probab.* **17**(103), 1–30.

[3] Bogard D G and Tiederman W G 1986 *J. Fluid Mech.* **162**, 389–413.

[4] Cantwell B J 2008 *Phys. Fluids A* **5**, 1993.

[5] Christensen K T and Adrian R J 2001 *J. Fluid Mech.* **431**, 433–443.

[6] Chung D and McKeon B J 2010 *J. Fluid Mech.* **661**, 341–364.

[7] Clauser F H 1956 *Adv. Mech.* **4**, 1–51.

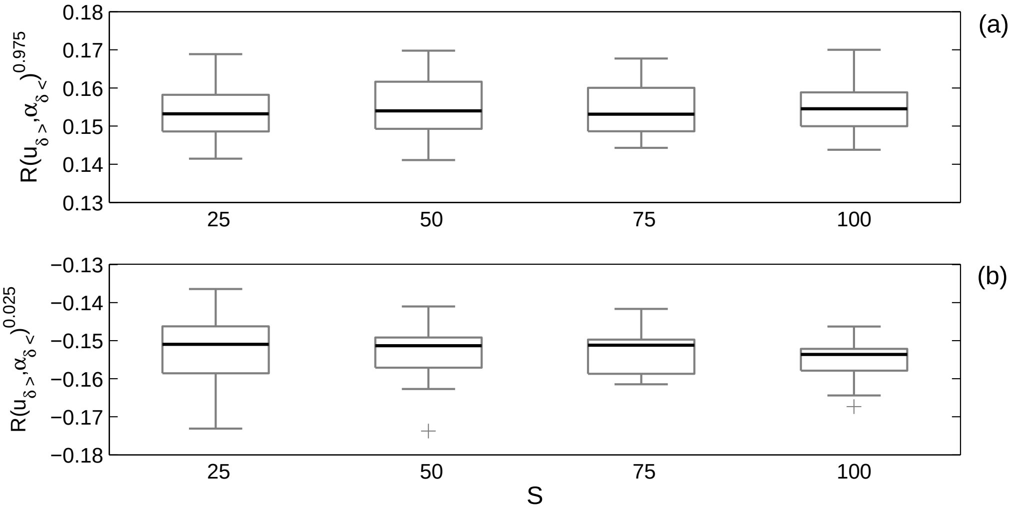

FIG. 11. Boxplots of the values for the bootstrapped confidence intervals over 20 estimates, each formed from S surrogates. The central bar indicates the median, with the lower and upper edges of the box at the first and third quartiles. The whiskers extend up to 1.5 times the quartile deviation from the edge of the box. Outlier data beyond this range are shown by a +'.

[8] Daubechies I 1992 *Ten Lectures on Wavelets* SIAM, Philadelphia.

[9] Frisch U and Parisi G 1985 *in* M Ghil, R Benzi and G Parisi, eds, 'Turbulence and Predictability in Geophysical Fluid Dynamics and Climate Dynamics' North Holland pp. 84–88.

[10] Frisch U, Sulem P L and Nelkin M 1978 *J. Fluid Mech.* **87**, 719–736.

[11] Ganapathisubramani B, Hutchins N, Hambleton W T, Longmire E K and Marusic I 2005 *J. Fluid Mech.* **524**, 57–80.

[12] Ganapathisubramani B, Hutchins N, Monty J P, Chung D and Marusic I 2012 *J. Fluid Mech.* **712**, 61–91.

[13] Ganapathisubramani B, Longmire E K and Marusic I 2003 *J. Fluid Mech.* **478**, 35–46.

[14] Guala M, Metzger M and McKeon B J 2011 *J. Fluid Mech.* **666**, 573–604.

[15] Herbin E and Lévy-Véhel J 2009 *Stoch. Proc. Appl.* **119**, 2277–2311.

[16] Hosokawa I 2007 *Progr. Theor. Phys.* **118**, 169–173.

[17] Hutchins N and Marusic I 2007*a* *J. Fluid Mech.* **579**, 467–77.

[18] Hutchins N and Marusic I 2007*b* *Phil. Trans. R. Soc. A* **365**, 647–664.

[19] Hutchins N, Monty J P, Ganapathisubramani B, Ng H and Marusic I 2011 *J. Fluid Mech.*

673, 235–285.

[20] Jaffard S 1997 *SIAM J. Math. Anal.* **28**, 944–970.

[21] Jiménez J 2012 *Ann. Rev. Fluid Mech.* **44**, 27–45.

[22] Kahalerras H, Malécot Y, Gagne Y and Castaing B 2007 *Phys. Fluids* **10**, 910–921.

[23] Keylock C J 2007 *Physica D* **225**, 219–228.

[24] Keylock C J 2008 *Geophys. Res. Lett.* **35**, art. no. L11804.

[25] Keylock C J 2009 *Env. Fluid Mech.* **9**, 509–523.

[26] Keylock C J 2010 *Nonlin. Proc. Geoph.* **17**, 615–632.

[27] Keylock C J, Nishimura K and Peinke J 2012 *J. Geophys. Res.* **117**, art. no. F01037.

[28] Keylock C J, Singh A and Foufoula-Georgiou E 2013 *Geophys. Res. Lett.* **40**, 10.1002/grl.50337.

[29] Keylock C J, Singh A, Venditti J and Foufoula-Georgiou E 2014 *Earth Surf. Proc. Land.* **39**, 1717–1728.

[30] Kline S J, Reynolds W C, Schraub F A and Runstadler P W 1967 *J. Fluid Mech.* **30**, 741–773.

[31] Kolmogorov A N 1941 *Dokl. Akad. Nauk. SSSR.* **30**, 299–303.

[32] Kolmogorov A N 1962 *J. Fluid Mech.* **13**, 82–85.

[33] Kolwankar K M and Lévy Vehel J 2002 *J. Fourier Analy. Appl.* **8**, 319–334.

[34] Kreuz T, Mormann F, Andrzejak R G, Kraskov A, Lehnertz K and Grassberger P 2007 *Physica D* **225**, 29–42.

[35] Ligrani P M and Bradshaw P 1987 *Exp. Fluids* **5**, 407–417.

[36] Lu S S and Willmarth W W 1973 *J. Fluid Mech.* **60**, 481–511.

[37] Marusic I, Mathis R and Hutchins N 2010 *Science* **329**, 193–196.

[38] Meneveau C and Sreenivasan K 1991 *J. Fluid Mech.* **224**, 429–484.

[39] Muzy J F, Bacry E and Arnéodo A 1991 *Phys. Rev. Lett.* **67**, 3515–3518.

[40] Naso A, Chertkov M and Pumir A 2006 *J. Turbulence* **7**(41).

[41] Nickels T B, Marusic I, Hafez S and Chong M S 2005 *Phys. Rev. Lett.* **95**, art. no. 074501.

[42] Nickels T B, Marusic I, Hafez S, Hutchins N and Chong M S 2007 *Phil. Trans. R. Soc. Lond.* **265**, 807–822.

[43] Nicolleau F and Vassilicos J C 1999 *Phil. Trans. R. Soc. Lond., Ser. A* **357**, 2439–2457.

[44] Ooi A, Martin J, Soria J and Chong M S 1999 *J. Fluid Mech.* **381**, 141–174.

[45] Peltier R F and Levy Véhel J 1995 Multifractional Brownian motion: Definition and preliminary results Technical Report 2645 INRIA, France.

[46] Percival D B and Walden A T 2000 *Wavelet Methods for Times Series Analysis* Cambridge University Press Cambridge, U.K.

[47] Perry A E and Chong M S 1987 *Annu. Rev. Fluid Mech.* **19**, 125.

[48] Pinton J F and Labbé R 1994 *J. Phys. II* **4**, 1461–1468.

[49] She Z S and Leveque E 1994 *Phys. Rev. Lett.* **72**, 336–339.

[50] Stresing R and Peinke J 2010 *New J. Phys.* **12**, art. no. 103046.

[51] Tomkins C D and Adrian R J 2003 *J. Fluid Mech.* **490**, 37–74.

[52] Townsend A A 1976 *The Structure of Turbulent Shear Flow* Cambridge University Press.

[53] Tsinober A, Shtilman L and Vaisburd H 1997 *Fluid Dyn. Res.* **21**, 477–494.

[54] Vieillefosse P 1984 *Physica A* **125**, 150–162.

[55] von Karman T and Howarth L 1938 *Proc. R. Soc. London, Ser. A* **164**, 192.